

**This Page Is Inserted by IFW Operations
and is not a part of the Official Record**

BEST AVAILABLE IMAGES

Defective images within this document are accurate representations of the original documents submitted by the applicant.

Defects in the images may include (but are not limited to):

- **BLACK BORDERS**
- **TEXT CUT OFF AT TOP, BOTTOM OR SIDES**
- **FADED TEXT**
- **ILLEGIBLE TEXT**
- **SKEWED/SLANTED IMAGES**
- **COLORED PHOTOS**
- **BLACK OR VERY BLACK AND WHITE DARK PHOTOS**
- **GRAY SCALE DOCUMENTS**
- **BLANK PAGES**

IMAGES ARE BEST AVAILABLE COPY.

**As rescanning documents *will not* correct images,
please do not report the images to the
Image Problem Mailbox.**

Jin-Kuo Ho, et al.
Application No.: 09/388,265
Page 2

PATENT

REMARKS

Claims 8-27 are pending.

Applicant notes with appreciation that claims 8-15 are allowed.

Claims 16, 18-20 and 22-24 stand rejected under 35 U.S.C. 102(b) as being unpatentable over Yamazaki (PN 4,559,552).

Claims 17 and 26 stand rejected under 35 U. S.C. 103(a) as being unpatentable over Yamazaki (PN 4,559,552) in view of Nakamura et al. (PN 5,563,422).

These rejections are respectfully traversed and reconsideration is respectfully requested.

Applicant has amended claim 16 to more clearly identify a novel aspect of the present invention. Specially, claim 16 has been amended to recite that the ohmic contact comprises a layer of p-type semiconductor oxide and a conductive layer. Support for this amendment may be found on page 9, line 23 to page 10, lines 1-5 and page 10 lines 15-17. In addition, this embodiment of the present invention is illustrated in Fig. 2 of the application. Also, applicants provide 5 references (see attachments) as evidence that the semiconductor oxide (tin oxide) disclosed in Yamazaki (PN 4,559,552) is n-type SnO₂ (stannic oxide), different from the p-type semiconductor oxide (SnO or stannous oxide) in the present invention.

35 U.S.C. 102(b) Rejections

Claims 16, 18-20 and 22-24 were rejected under 35 U.S.C. 102(b) as being anticipated by Yamazaki (U. S. Patent No. 4,559,552, of record).

With reference to Figure 8 and col. 10, lines 38-42; and col. 13, lines 1-8 of U.S. Pat. No. 4,559,552, it is respectfully submitted that Yamazaki teaches an electrode (61) in a semiconductor device, formed on a semiconductor material (5). The electrode (61) includes a light transparent conductive layer (64), such as tin oxide, and a reflective conductive layer (63). However, Yamazaki does not anticipate claim 16 because it does not teach or suggest a layer of p-type semiconductor oxide and a

Jin-Kuo Ho, et al.
Application No.: 09/388,265
Page 3

PATENT

conductive layer. It should be noted that tin oxide (SnO_2) is n-type, not p-type. The conductivity type will be illustrated as follows.

In response to applicant's arguments, the Examiner states that tin oxide of Yamazaki is p-type semiconductor oxide, having the same material as that of the present invention (SnO). It is respectfully submitted that the Examiner's viewpoint (tin oxide is inherent p-type) is incorrect. Herein, applicants provide references (see attachments) as evidence that the semiconductor oxide (tin oxide) disclosed in Yamazaki (PN 4,559,552) is n-type SnO_2 (stannic oxide), different from the p-type semiconductor oxide (SnO or stannous oxide) disclosed in the present invention.

Table. 1 lists information for SnO_2 and SnO .

Table 1

Formula	SnO_2	SnO
Material name	Stannic oxide	Stannous oxide
Chemical name	Tin oxide	Tin monoxide
Oxidation state	+4	+2
Conductivity type	n-type	p-type

With reference to Attachment 1, both undoped and antimony-doped tin oxide (SnO_2) films having the electron conduction mechanism are verified. Thus, undoped and antimony-doped tin oxide films are n-type semiconductor oxide. The above result is also verified by Attachment 2 and Attachment 3. Moreover, table 17.6 in Attachment 4 clearly shows that tin oxide (SnO_2) is n-type semiconductor oxide and tin monoxide (SnO) is p-type semiconductor oxide. Thus, the metal oxides disclosed by Yamazaki are all n-type semiconductor oxides. Since Yamazaki does not teach all the limitations found in claim 16, it is respectfully submitted that claim 16 is not anticipated by this reference.

In addition, Yamazaki emphasizes that the transparent conductive layer (64) has good transparency and conductivity. That is, it is reasonable that tin oxide of the transparent conductive layer (64) is SnO_2 in U.S. Pat. No. 4,559,552, because SnO has a worse transparency and lower conductivity, (see Attachment 5 and Attachment 2).

Jin-Kuo Ho, et al.
Application No.: 09/388,265
Page 4

PATENT

Thus, the prior art does not describe or suggest all the elements of the present invention as set forth in independent claim 16 of the present invention, and therefore cannot anticipate these claims under 35 U.S.C. 102(b).

As previously noted, Yamazaki does not anticipate claim 16 because it does not teach an ohmic contact comprising a p-type semiconductor oxide layer and a conductive layer. In electrode 61 of the prior art, a light transparent conductive layer 64 is formed of a metal oxide consisting of n-type tin oxide, as opposed to a p-type semiconductor oxide. That is, none of the materials contained in layers 63 and 64 are p-type semiconductor oxides. Applicant emphasizes that SnO (stannous oxide/tin monoxide) used in the present invention is p-type, thereby obtaining a much lower interface resistivity of $1.0 \times 10^{-4} \Omega \text{ cm}$. Further, since p-type semiconductor oxide and n-type semiconductor oxide have different conduction mechanisms, Yamazaki cannot make the present invention obvious under 35 U.S.C. 103.

Nakamura does not make up for the lack of teaching in Yamazaki because it does not teach an ohmic contact comprising a p-type semiconductor oxide layer and a conductive layer. Thus, the prior art cannot make the present invention obvious under 35 U.S.C. 103, as there is no suggestion for an ohmic contact comprising a layer of p-type semiconductor oxide and a conductive layer.

For the reasons mentioned above, Yamazaki does not teach a layer of p-type semiconductor oxide. It is therefore applicants' belief that claim 16 is allowable over the cited art. Insofar as claims 17-27 depend from claim 16, it is applicants' belief these claims are also allowable.

Accordingly, it is respectfully submitted that claim 16 and all claims dependent thereon are allowable over the prior art. Reconsideration and withdrawal of the pending grounds of rejection are therefore respectfully requested.

For all of these reasons, applicant submits that this application is now in condition for allowance. Prompt issuance of a Notice of Allowance is earnestly solicited.

Jin-Kuo Ho, et al.
Application No.: 09/388,265
Page 5

PATENT

References:

Attachment 1:

E. Shanthi et al.

J. Appl. Phys., vol. 51, December 1980, pp. 6243-6251 "Electrical and optical properties of undoped and antimony-doped tin oxide films"

Attachment 2:

R. G. Goodchild et al.

J. Appl. Phys., vol. 57, March 1985, pp. 2308-2310

"Electrical properties of highly conducting and transparent thin films of magnetic sputtered SnO_2 "

Attachment 3:

John Robertson

The American Physical Society, Physical Review B., vol. 30, September 1984, pp. 3520-3522

"Defect levels of SnO_2 "

Attachment 4:

W.D. Kingery, H.K. Bowen and D.R. Uhlmann

"Introduction to Ceramics" John Wiley & Sons, pp. 888-897, New York (1975), especially referring to Table 17.6

Attachment 5:

Bertil. et al.

J. Appl. Phys., vol. 68, August 1990, pp. 6241-6245

"Characterization of re-sputtered SnO_x thin films by electron microscopy, Hall-effect measurement and Mossbauer spectrometry"

Jin-Kuo Ho, et al.
Application No.: 09/388,265
Page 6

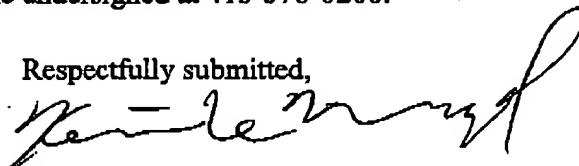
PATENT

CONCLUSION

In view of the foregoing, Applicants believe all claims now pending in this Application are in condition for allowance. The issuance of a formal Notice of Allowance at an early date is respectfully requested.

If the Examiner believes a telephone conference would expedite prosecution of this application, please telephone the undersigned at 415-576-0200.

Respectfully submitted,



Kevin T. LeMond
Reg. No. 35,933

TOWNSEND and TOWNSEND and CREW LLP
Two Embarcadero Center, 8th Floor
San Francisco, California 94111-3834
Tel: 415-576-0200
Fax: 415-576-0300
KTL:blj
SF 1432504 v1

Jin-Kuo Ho, et al.
Application No.: 09/388,265
Page 7

PATENT

VERSION WITH MARKINGS TO SHOW CHANGES MADE

- 1 16. (Twice Amended) An ohmic contact in a semiconductor device,
- 2 which is formed on a p-type semiconductor material, the ohmic contact comprising a
- 3 layer of p-type semiconductor oxide and a conductive layer.

SF 1432504 v1

JAN-13-2003 MON 15:15

FAX NO.

31 DEC 2002 15:27

NO. 287 P. 9/17

Attachment 1

Electrical and optical properties of undoped and antimony-doped tin oxide films

E. Shanthi, V. Dutta, A. Banerjee, and K. L. Chopra

Department of Physics, Indian Institute of Technology, Delhi, New Delhi 110016, India

(Received 4 February 1990; accepted for publication 12 May 1990)

Tin oxide films have been prepared on glass substrates by spray pyrolysis technique. The electrical and optical properties of undoped and antimony-doped tin oxide films have been studied. The temperature dependence of electron mobility has been analyzed to establish the electron conduction mechanism. Optical properties near the plasma edge have been analyzed using Drude's theory. The dependence of effective mass on carrier concentration has been explained on the basis of nonparabolicity of the conduction band. The shift in the Fermi energy, calculated on the basis of energy dependent effective mass, is consistent with the measured shift in the absorption edge.

PACS numbers: 72.20.Jv, 72.80.Ey, 68.55.+b

1. INTRODUCTION

Doped tin oxide films are being extensively studied, since their high optical transmission, electrical conduction, and infrared reflection have great potential for applications in optoelectronic devices, hybrid microelectronics, and photo-thermal conversion of solar energy. Tin oxide films have been prepared by various techniques such as chemical vapor deposition,^{1,2} spray pyrolysis,^{3,4} vacuum evaporation,⁵ sputtering,⁶ and by dc glow discharge.⁷ The properties of the films have been found to depend strongly on the mode of preparation. It has been found that the spray technique is most suitable for obtaining films of high optical transmission and low sheet resistance. Further, spray technique is inexpensive and ideally suited for large area substrate applications.

Work on tin oxide films has resulted in a lot of measured data⁸⁻¹³ on the properties of undoped and antimony doped tin oxide films. However, a consistent picture of the prevailing electrical conduction mechanism¹⁴ has not yet been established and needs further investigation. Moreover, effect of antimony doping on electrical and optical properties of tin oxide films is not clearly understood. Hence we have carried

out a detailed and systematic investigation on undoped and antimony-doped tin oxide films. In this paper we report the structural, electrical, and optical properties of undoped and antimony-doped tin oxide films.

2. EXPERIMENTAL DETAILS

Tin oxide films were prepared by using alcoholic solutions of stannic chloride, on glass substrates held at temperatures ranging between 340–540 °C. A typical spray mixture consists of 0.7-M SnCl₄, 10-M propanol and 0.2-M HCl, with varying concentration of SbCl₃. The pH of the solution is ~0.3. The temperature of the substrates was monitored by chromel-alumel thermocouple fixed on top surface of the substrate. The variation of the substrate temperature during spray was maintained within $\pm 5^\circ\text{C}$ with the help of a temperature controller. Compressed air at a pressure of $\sim 0.5\text{ kg/cm}^2$ was used as the carrier gas and the spray rate was $\sim 10\text{ cm}^3/\text{min}$. The schematic diagram of the spray set up is shown in Fig. 1.

The microstructural details and the grain size of the films prepared on rock salt crystals were determined using transmission electron micrographs. The surface morphology of the films was examined in a Cambridge S4-10 scanning electron microscope. The thickness of the films was measured by etching the films¹⁵ with Zn dust in hydrochloric acid and measuring the height of the resulting step in a height measuring instrument (Talystep). All the measurements were carried out on films of the same thickness ($\sim 3500\text{ \AA}$). van der Pauw's technique was employed to measure the electrical resistivity and Hall coefficient of the films. Temperature dependence of resistivity and carrier concentration was measured in a vacuum of $\sim 10^{-5}\text{ Torr}$.

Transmission and reflection in the wavelength range 0.22–1.0 μm were measured using a Pye Unicam SP 700A double beam spectrophotometer. Measurements in the infrared range 1.0–10 μm were made in a Grubb Parson MK III spectrophotometer.

3. RESULTS AND DISCUSSION

A. Structural properties

Electron diffraction patterns of undoped and antimo-

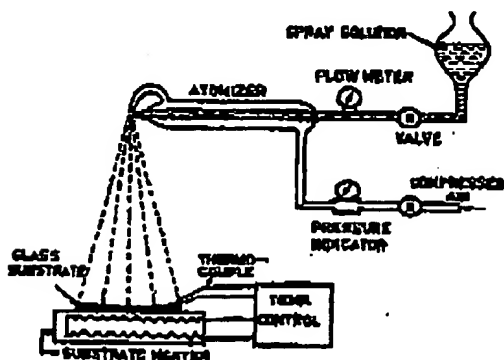


FIG. 1. Schematic diagram of the experimental setup for spray deposition of tin oxide films.

JAN-13-2003 MON 15:16

FAX NO.

31.DEC.2002 15:26

NO.207 P.10/17



FIG. 1. (a) Electron diffraction pattern of undoped tin oxide film and transmission electron micrographs of (b) undoped tin oxide film and (c) 1.4-at% antimony-doped tin oxide film.

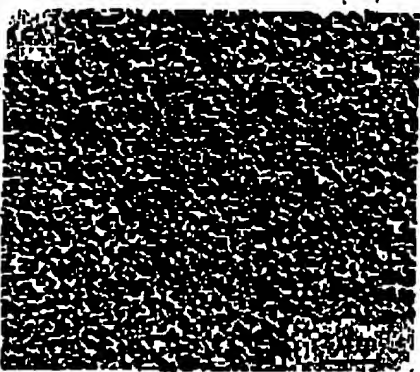
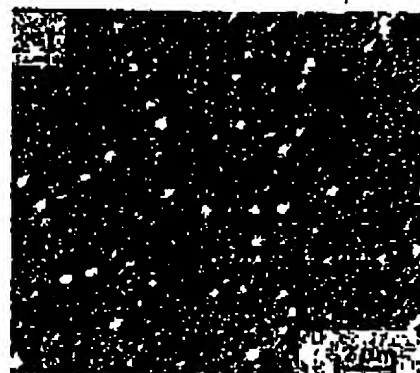


FIG. 2. Scanning electron micrographs of undoped tin oxide films prepared at three different substrate temperatures: (a) 210°C, (b) 440°C, and (c) 540°C.

31.DEC.2002 15:26

NO.287

P.11/17

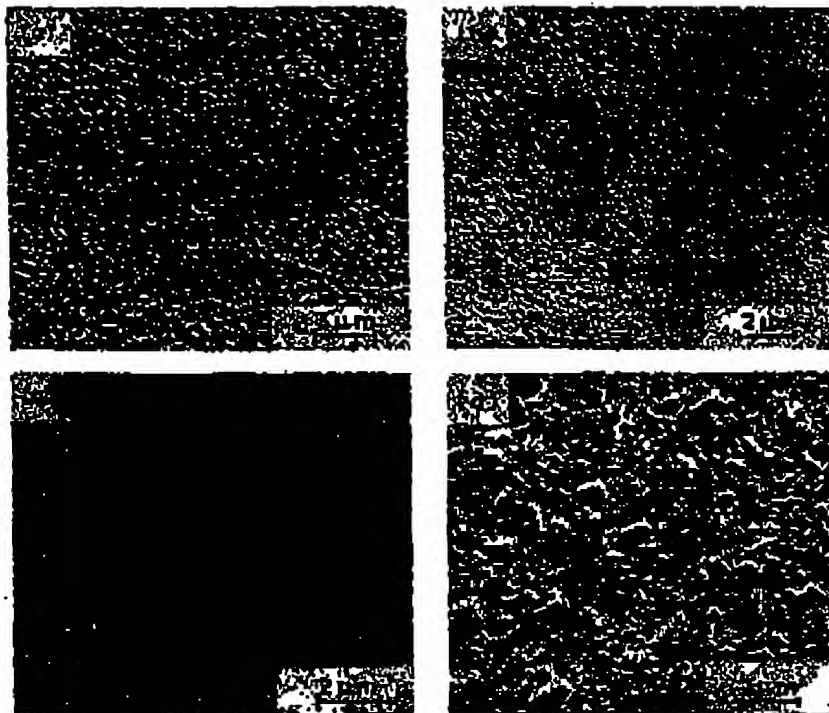


FIG. 4. Scanning electron micrographs of antimony-doped tin oxide films: (a) 0.7-m/o, (b) 1.4-m/o, (c) 3-m/o, and (d) 10-m/o.

xy-doped tin oxide films [Fig. 2(a)] prepared at $\sim 540^\circ\text{C}$ show that these are polycrystalline and are of irregular structure. The lattice parameters of these films correspond to that of bulk tin oxide. It has been found that grain size of the undoped tin oxide films is $\sim 250\text{ \AA}$ which increases to $\sim 600\text{ \AA}$ on addition of antimony up to 1.4-m/o, as shown in the micrographs [Figs. 3(b) and 3(c)]. Further increase in antimony concentration does not lead to any appreciable change in the grain size.

The surface topography of the undoped tin oxide films is shown in the scanning electron micrographs [Figs. 3(a), 3(b), and 3(c)] for three different substrate temperatures 340, 440, and 540°C , respectively. At the lower temperature of deposition ($\sim 340^\circ\text{C}$) small particles of $\sim 0.4\text{ }\mu\text{m}$ in size are scattered over a smooth background. These particles vanish as the temperature increases [Figs. 3(b) and 3(c)] and the background becomes coarse. Figures 4(a), 4(b), 4(c), and 4(d) show the surface topography of the oxide films, prepared at 540°C , with 0.7, 1.4, 3, and 10-m/o antimony concentration, respectively. With increasing antimony concentration up to 3-m/o, the surface becomes smooth. At high antimony concentration of 10-m/o, the surface becomes coarse and small particles of $\sim 0.7\text{ }\mu\text{m}$ in size appear on the surface.

B. Electrical properties

Hall measurements show that both undoped and antimony-doped tin oxide films are n-type semiconductors. Fig.

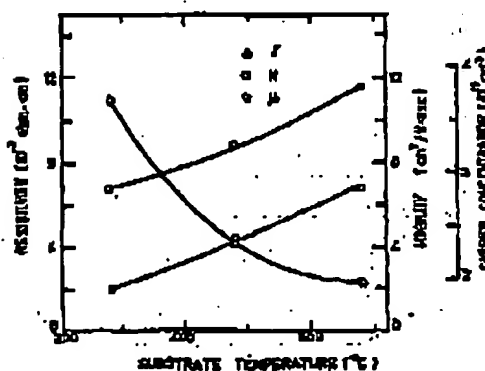


FIG. 5. Variation of resistivity ρ , mobility μ , and carrier concentration n in undoped tin oxide films with substrate temperature.

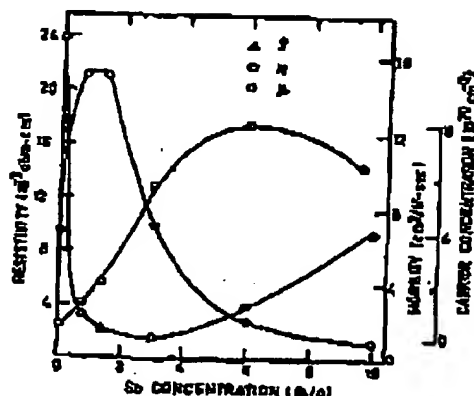


FIG. 6. Variation of resistivity ρ , mobility μ , and concentration N in the oxide films with antimony concentration.

ure 5 shows the variation of carrier concentration N , resistivity ρ , and mobility μ of free carriers (measured at room temperature) as a function of substrate temperature. A gradual decrease in the resistivity occurs on raising the temperature of deposition from 340 to 540 °C. On the other hand, the carrier concentration and mobility show an increase with substrate temperature, the variation in the mobility being larger than the variation in the carrier concentration. It has been observed that the transmission of the films improves from 77 to 84% (measured at 0.7 μ m) on increasing the temperature of deposition from 340 to 540 °C. Since substrate temperature of 540 °C produces the best values of electrical conductivity and optical transmission, all the subsequent studies have been carried out on the films prepared at ~540 °C.

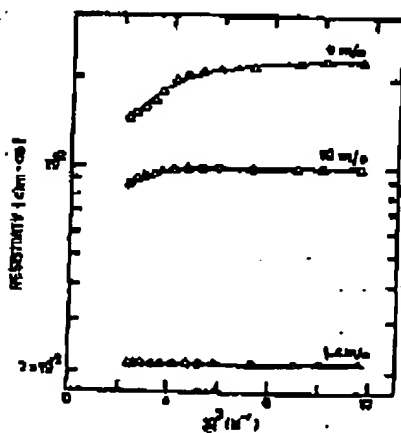


FIG. 7. Resistivity ρ of undoped and antimony-doped tin oxide films as a function of reciprocal temperature.

6240 J. Appl. Phys., Vol. 91, No. 12, December 2000

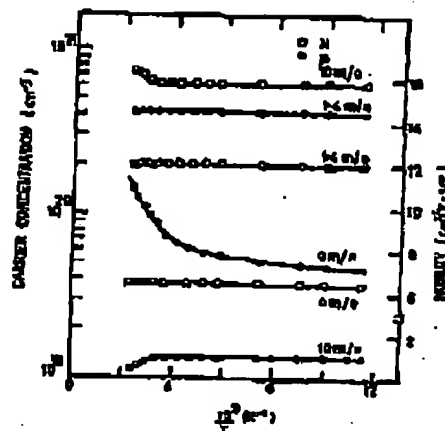


FIG. 8. Temperature dependence of mobility μ and carrier concentration N of undoped and antimony-doped tin oxide films.

Figure 6 shows the variation of the resistivity, carrier concentration, and mobility with antimony concentration. Resistivity decreases up to a concentration of 3-m/o and starts increasing for higher Sb concentrations. The carrier concentration, however, shows a steep increase initially up to 6-m/o and a gradual decrease thereafter. Mobility shows a peak at ~1.4-m/o Sb concentration.

Figures 7 and 8 show the dependence of the resistivity, carrier concentration, and mobility on temperature (85–430 K) for undoped, 1.4- and 10-m/o Sb-doped tin oxide films. The carrier concentration remains invariant in undoped and 1.4-m/o Sb-doped tin oxide films in the temperature range investigated, while it shows a slight increase above room temperature in 10-m/o Sb-doped films. Resistivity decreases above room temperature for undoped and 10-m/o Sb-doped tin oxide films, while it remains invariant in 1.4-m/o Sb-doped films.

The small increase in carrier concentration in undoped tin oxide films with deposition temperature is attributed to the increase in number of oxygen vacancies.¹⁰ On addition of Sb up to 6-m/o, carrier concentration increases as expected, since Sb forms a shallow donor level.³ However, at 10-m/o Sb concentration, there is a small decrease in carrier concentration. This is probably due to increased disorder which causes an increase in the activation energy of the donors.³ The invariance of carrier concentration with temperature in undoped and 1.4-m/o Sb-doped films indicates that the impurity band formed at the shallow donor level has merged with the conduction band. The increase in carrier concentration above room temperature, also observed by Inagaki *et al.*,¹¹ in 10-m/o Sb-doped films is not explainable.

In order to analyze the mobility data, the contribution of the different scattering mechanisms to mobility is separated by using Matthiessen's rule,¹² provided the magnitude of the effects of any two mechanisms are not comparable. The

Ghoshal *et al.* 6245

31.DEC.2002 15:29

NO.287 P.13/17

observed mobility μ_{obs} is, then, given by

$$\frac{1}{\mu_{\text{obs}}} = \frac{1}{\mu_{\text{opt}}} + \frac{1}{\mu_i} + \frac{1}{\mu_g},$$

which includes the effects of optical lattice scattering μ_{opt} , ionized impurity scattering μ_i , and the grain boundary scattering μ_g . The contributions due to other scattering mechanisms, e.g., acoustic lattice scattering and neutral impurity scattering, are neglected.

The contributions due to ionized impurity scattering and optical lattice scattering have been calculated, using formulas for degenerate semiconductors, by Mott²¹ and Howarth and Sondheimer,²¹ respectively. The effective mass of electrons has been taken to be 0.1 m_0 as determined from plasma edge measurements. It is found that the contributions due to these two scattering mechanisms are small. This is expected since the mobility ($\sim 7 \text{ cm}^2/\text{V sec}$) of carriers in the oxide film is small as compared to the corresponding single-crystal values of $\sim 90 \text{ cm}^2/\text{V sec}$ ^{22,23} for approximately the same carrier concentration. It can therefore be concluded that grain boundary scattering is the dominant scattering mechanism limiting the mobility. This is further confirmed by analyzing the temperature dependence of the mobility. Following Parshin's model,²⁴ grain boundary scattering dependent mobility is given by

$$\mu = AT^{-1/2} \exp[-(eV_g/kT)],$$

where V_g is the potential barrier for scattering at the grain boundary; the other symbols have their usual significance. As shown in Fig. 9, the plot of $\ln(\mu T^{1/2})$ vs $1/T$ is a straight line. The potential barrier V_g , calculated from the slope of the straight line, yields a value of $\sim 30 \text{ meV}$.

The dependence of the mobility on deposition temperature (Fig. 5) can also be understood on the basis of grain boundary scattering. The grain size increases with deposition temperature,¹³ causing a concurrent decrease in grain

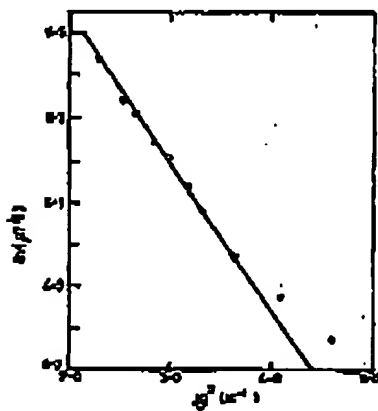


FIG. 9. Plot of $\ln(\mu T^{1/2})$ vs reciprocal temperature of undoped tin oxide films.

6267 J. Appl. Phys., Vol. 91, No. 12, December 1990

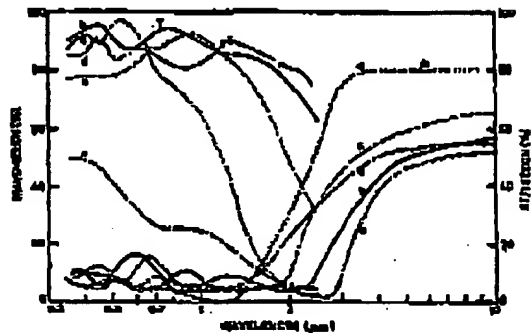


FIG. 10. Transmittance and reflection spectra of films with different antimony concentration: (a) 0 cm³/m, (b) 0.7 cm³/m, (c) 1.4 cm³/m, (d) 3 cm³/m, and (e) 10 cm³/m.

boundary potential V_g . Hence, with increasing deposition temperature, the grain boundary scattering decreases, giving a corresponding increase in mobility.

Our conclusions contradict those of Tsai *et al.*,⁹ who on the basis of thermoelectric power measurements, have inferred that ionized impurity scattering is the predominant scattering mechanism at room temperature. However, their conclusion is questionable, as the experimental values of the thermoelectric power measured at room temperature does not agree well with the computed value. The disparity between these two values clearly indicates the presence of some other scattering mechanism, which, we contend, is the grain boundary scattering. The contribution from grain boundary scattering to thermoelectric power is difficult to assess.

With a further increase in antimony concentration, ionized impurity scattering is expected to dominate, thereby decreasing the mobility of free carriers. However, the increase in the mobility, with increase in Sb concentration up to 1.4 m/o, shows that ionized impurity scattering is not predominant since mobility would have decreased in such a case. On the other hand, the increase in the grain size from $\sim 350 \text{ \AA}$ for undoped tin oxide films to $\sim 600 \text{ \AA}$ for 1.4-m/o Sb-doped films indicates that the grain boundary scattering reduces, resulting in an increase in the mobility. The observed decrease in mobility beyond this concentration of antimony can be attributed to the increase in contribution from ionized impurity scattering.

C. Optical properties

The transmission in the wavelength range 0.33 to 2.0 μm and reflection in the range 0.33 to 10.0 μm for undoped and doped tin oxide films are shown in Fig. 10. The reflection for undoped tin oxide films, in which the plasma resonance occurs at $\sim 3.2 \mu\text{m}$, was measured in films prepared on quartz substrates. The transmission of these films remains high ($\sim 80\%$) over a large wavelength range from 0.4 to 2.0 μm . In doped tin oxide films, transmission increases initially up to 1.4-m/o Sb concentration and thereafter decreases with further addition of antimony. Plasma resonance occurs in the near infrared region owing to high concentra-

Chang *et al.* 6267

tion ($\sim 10^{20}/\text{cm}^3$) of free carriers in the films. The reflection in infrared region increases with increasing Sb concentration up to 3-m/o. This is understandable, since the magnitude of reflection depends upon mobility and carrier concentration¹² and surface topography of the films. With increasing Sb concentration, N and μ increase and the surface of the films also becomes smoother [compare Figs. 4(a), 4(b), and

4(c)], which accounts for the increase in infrared reflection up to 3-m/o. The decrease in reflection in 10-m/o Sb-doped films may be due to the low value of mobility and coarse surface of the films.

Figure 11 depicts the variation of refractive index n and extinction coefficient k of undoped and doped tin oxide films with photon energy, which are computed from transmission and reflection data using the following formulae¹³:

$$T = \frac{n_2}{n_0} \frac{[(1+g_1)^2 + h_1^2][(1+g_2)^2 + h_2^2]}{g_1^2 + (g_1^2 + h_1^2)e^{-2\alpha_1} + C \cos 2\gamma_1 + D \sin 2\gamma_1} \quad (1)$$

$$R = \frac{(g_1^2 + h_1^2)e^{-2\alpha_1} + (g_2^2 + h_2^2)e^{-2\alpha_2} + A \cos 2\gamma_1 + B \sin 2\gamma_1}{g_1^2 + (g_1^2 + h_1^2)e^{-2\alpha_1} + C \cos 2\gamma_1 + D \sin 2\gamma_1} \quad (2)$$

where

$$g_1 = \frac{n_0^2 - n_1^2 - k_1^2}{(n_0 + n_1)^2 + k_1^2}, \quad g_2 = \frac{n_1^2 - n_2^2 + k_2^2}{(n_1 + n_2)^2 + k_2^2}, \quad h_1 = \frac{2n_0k_1}{(n_0 + n_1)^2 + k_1^2}, \quad h_2 = \frac{-2n_2k_2}{(n_1 + n_2)^2 + k_2^2},$$

$$\alpha_1 = \frac{2\pi k_1 d}{\lambda}, \quad \gamma_1 = \frac{2\pi n_1 d}{\lambda},$$

and $A = 2(g_1g_2 + h_1h_2)$, $B = 2(g_1h_2 - g_2h_1)$, $C = 2(g_1g_2 - h_1h_2)$, $D = 2(g_1h_2 + g_2h_1)$. $n_1 - ik_1$ represents the complex refractive index of the films of thickness d , and n_2 represents that of glass substrate, the extinction coefficient being zero in the wavelength range investigated. The extinction coefficient increases while refractive index of the films decreases near plasma edge and is found to depend on the doping concentration (see Fig. 11).

To describe the optical phenomenon near infrared region the classical Drude theory can be used, since the carrier concentration in these films is $\sim 10^{20}/\text{cm}^3$. The plasma reso-

nance frequency ω_p is then determined from the spectral dependence of real and imaginary parts of the dielectric constant, which are given by

$$\epsilon' = n^2 - k^2 = \epsilon_\infty \left(1 - \frac{\omega_p^2}{\omega^2 + \gamma^2}\right) \quad (3)$$

and

$$\epsilon'' = 2nk = \frac{\omega_p^2 \gamma \omega}{\omega(\omega^2 + \gamma^2)} \quad (4)$$

where ϵ_∞ and ϵ_0 represent the dielectric constants of the medium and of free space, respectively, and

$$\omega_p = (4\pi N e^2 / \epsilon_0 \epsilon_\infty m)^{1/2} \quad (5)$$

is the plasma resonance frequency, m denotes the mass of charge carriers in the conduction band, and $\gamma = 1/\tau$, where τ is the relaxation time which is obtained by comparing ϵ''

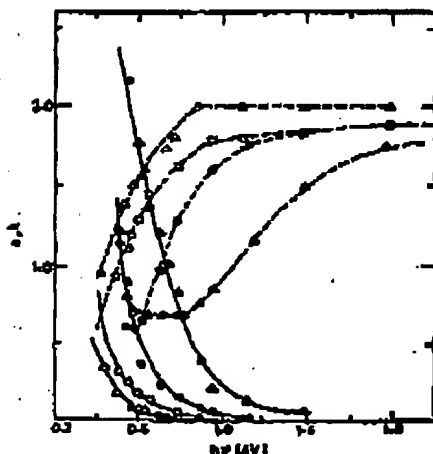


FIG. 11. Refractive index n (solid line) and extinction coefficient k (dashed line) of undoped and antimony-doped tin oxide films as a function of photon energy. Films with different antimony content are denoted by \circ , \square , \bullet , \triangle 0, 0.7, 1.4, and 3-m/o.

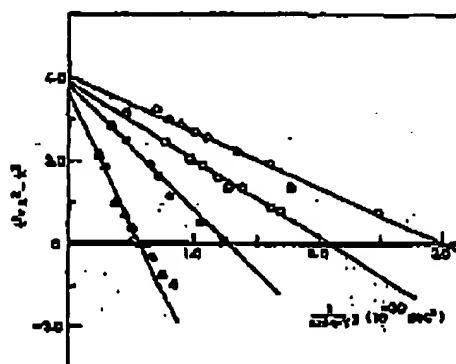


FIG. 12. Dependence of ϵ' on $1/(\omega^2 + \gamma^2)$ of films with different antimony concentrations \circ , \square , \bullet , \triangle 0, 0.7, 1.4, and 3-m/o.

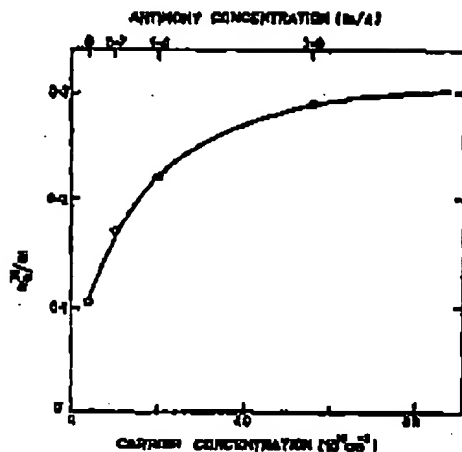


FIG. 13. Calculated value of effective state of electrons (n/m) as a function of carrier concentration and undoped concentration.

and ϵ'' . Near the plasma edge, the ϵ' versus $1/(\omega^2 + \gamma^2)$ plot (Fig. 12) is a straight line indicating the validity of the Drude theory. The plasma resonance frequency is obtained from this plot at $\epsilon'' = 0$. The threshold of the plasma edge was found to shift to a shorter wavelength from $\sim 3.2 \mu\text{m}$ for undoped tin oxide films to $\sim 1.3 \mu\text{m}$ for 3-m/o Sb-doped films, as expected.

The effective mass of free carriers at different Sb concentration is obtained from Eq. (5) with the known plasma resonance frequency and carrier concentration. It is found to

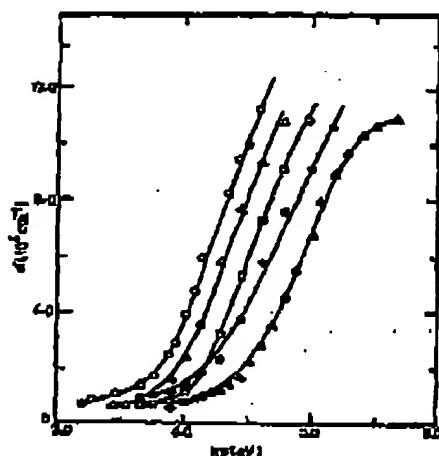


FIG. 14. Variation of absorption coefficient α with photon energy for different carrier concentrations: \square — $N = 10^{19}/\text{cm}^3$, Δ — $N = 5 \times 10^{19}/\text{cm}^3$, \square — $N = 1.5 \times 10^{20}/\text{cm}^3$, \oplus — $N = 2.7 \times 10^{20}/\text{cm}^3$, and Δ — $N = 7.9 \times 10^{20}/\text{cm}^3$.

6249 J. Appl. Phys., Vol. 91, No. 12, December 1990

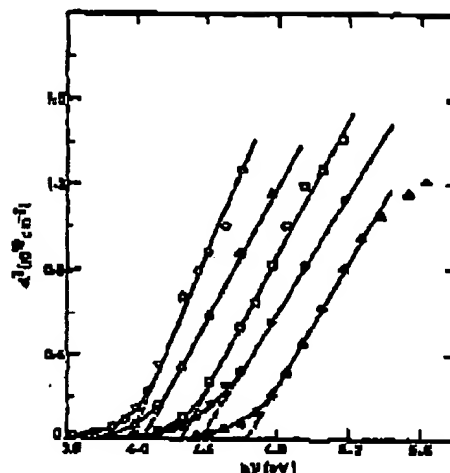


FIG. 15. Plot of α^2 vs photon energy for different carrier concentrations: \square — $N = 10^{19}/\text{cm}^3$, Δ — $N = 5 \times 10^{19}/\text{cm}^3$, \square — $N = 1.5 \times 10^{20}/\text{cm}^3$, \oplus — $N = 2.7 \times 10^{20}/\text{cm}^3$, and Δ — $N = 7.9 \times 10^{20}/\text{cm}^3$.

vary from 0.1 m for undoped tin oxide films to 0.29 m for 3-m/o Sb-doped films (Fig. 13). This is in agreement with the observation of Lyubchenko *et al.*¹⁴ Such a large change in effective mass indicates nonparabolicity of the conduction band.

For the determination of the fundamental absorption edge of undoped and doped films, which lies in ultraviolet range, the films were prepared on quartz substrate. The spectral dependence of the absorption coefficient $\alpha = 4\pi k/\lambda$ of these films near the ultraviolet range has been computed from transmission and reflection data using Eqs. (1) and (2) in the same manner as in infrared range. Figure 14 depicts α as a function of photon energy for different carrier concentrations. The nature of the transition involved can be determined on the basis of the dependence of α on $h\nu$. For allowed direct transition, α is given by

$$\alpha \propto (h\nu - E_g)^{1/2},$$

where E_g is the separation between the conduction band and the valence band at the same wave number (K). Figure 15 shows the variation of α^2 with $h\nu$, which is a straight line, indicating that the direct transition is the dominant transition involved. The energy gap is obtained by extrapolating the linear portion of the α^2 vs $h\nu$ plot to $\alpha = 0$. It may be noted that the fundamental absorption edge shifts from 3.95 eV for a carrier concentration of $\sim 10^{19}/\text{cm}^3$ to 4.61 eV corresponding to a carrier concentration of $7.9 \times 10^{20}/\text{cm}^3$. The shift in the fundamental absorption edge can be attributed to the Moss-Burstein shift,²⁰ which occurs owing to filling up of low lying energy levels by the conduction electrons.

Such a large shift in the absorption edge is consistent with the fact that tin oxide is a broad band semiconductor.^{21,22} Hence the variation in effective mass of electrons in

Green et al. 6249

the conduction band can be attributed to the nonparabolicity of the bands near the center of Brillouin zone. For nonparabolic bands, m_e^* is related to the band parameters¹⁰ by

$$\frac{1}{m_e^*} = \frac{1}{m_0 K_F} \left| \frac{\partial E}{\partial K} \right|_F \quad (6)$$

where the subscript F indicates that the quantity has to be evaluated at the Fermi level, since normally in nonparabolic bands m_e^* is dependent only upon the shape of energy bands near the Fermi level. K_F represents the magnitude of wave number at the Fermi level. Assuming spherical constant energy surfaces, we can obtain K_F corresponding to different carrier concentration from

$$N = \frac{2}{(2\pi)^3} \frac{4\pi K_F^3}{3} \quad (7)$$

Knowing m_e^* as a function of N from Fig. 13, the variation of m_e^* with K_F is obtained from Eq. (7) (see Fig. 14). Then, the following equation

$$\left| \frac{\partial E}{\partial K} \right|_F = \frac{E_F}{m_e^*(K_F)}$$

is numerically integrated to give the shift in Fermi level of doped films with respect to undoped tin oxide films as a function of ΔE_F . The exact position of the Fermi level with reference to the bottom of the conduction band can then be determined by adding the value corresponding to the Fermi level of degenerate tin oxide films. The latter is determined from the shift in the absorption edge measurements using the relation

$$E_g = E_g^0 + [1 + (m_e^*/m_0)](E_F - 4kT)$$

where E_g^0 is the band gap of nondegenerate tin oxide films ($N \approx 10^{17}/\text{cm}^3$), other parameters having the usual significance. Assuming $m_e^* = -0.9m_0$ (the reasons are explained later), the Fermi level of the degenerate undoped tin oxide films is found to be -0.19 eV above the conduction band minimum, which is in agreement with the observations of Arai¹⁰ for the same carrier concentration. Thus E_F as a function of K_F is obtained. A polynomial best fit shows the following dependence of E_F on K' ($K' = E_F/K_F$, where $K_F = 10^6 \text{ cm}^{-1}$):

$$E_F(\text{eV}) = -0.61 + 0.07K' - 4.96 \times 10^{-4}K'^2 + 1.15 \times 10^{-6}K'^3 \quad (8)$$

In order to confirm whether the values of Fermi energy are consistent with the Burstein shift obtained from absorption edge measurements, $h\nu$ is obtained from Fig. 14 for a given α for different carrier concentrations. This value of $h\nu$ is then compared with the calculated values of $h\nu(\alpha)$ obtained from the following equation:

$$h\nu(\alpha) = E_g + [1 + (m_e^*/m_0)]\{E_F - kT \ln[(\alpha_0 - \alpha)/\alpha]\}$$

where α_0 is the absorption coefficient for nondegenerate tin oxide films at the same photon energy obtained from Fig. 14, and the value of E_F is obtained from Eq. (8). A good agreement with the experimental value of $h\nu$ is obtained for $m_e^* = -0.9m_0$. The negative value of hole mass indicates that

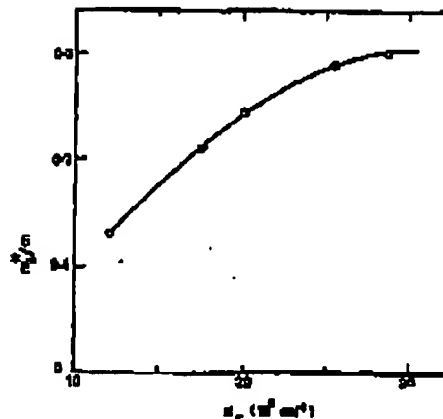


FIG. 14. Variation of effective mass of electrons (m_e^*/m_0) with wave number (K_F).

the valence band is curved in the same direction as the conduction band. It is to be noted that a similar type of analysis has been done by Spitzer and Fan¹⁰ on InSb.

IV. CONCLUSIONS

The variations of the electrical and optical properties of tin oxide films have been studied as a function of antimony concentration. It is found that grain boundary scattering is the dominant scattering mechanism limiting the mobility of free carriers at room temperature for undoped and 1.4-m/o Sb-doped films. The conduction band of tin oxide films is nonparabolic and a large Burstein shift is observed with Sb doping. On the basis of nonparabolicity of conduction bands, the dependence of energy on wave vectors has been established from the experimental data.

ACKNOWLEDGMENT

We thank Professor K. P. Jain for many useful discussions.

1. Kane, H. P., Sobushin, and W. Kern, *J. Electrochem. Soc.* **123**, 270 (1976).
2. J. Baliga and S. K. Ghosh, *J. Electrochem. Soc.* **123**, 941 (1976).
3. A. Rohatgi, T. R. Vignola, and L. H. Fleck, *J. Am. Ceram. Soc.* **57**, 273 (1974).
4. S. Kim and H. A. Lakshmin, *J. Am. Ceram. Soc.* **58**, 23 (1975).
5. H. Watanabe, *Jpn. J. Appl. Phys.* **9**, 1537 (1970).
6. W. Lohmann and H. Wagner, *Thin Solid Films* **27**, 359 (1973).
7. D. E. Constant, *J. Electrochem. Soc.* **122**, 1336 (1975).
8. L. H. Fleck, *J. Phys. Soc. Jpn.* **13**, 937 (1960).
9. K. Koch, *Phys. Status Solidi* **3**, 1039 (1967).
10. T. A. Aham, V. C. Marcano, and M. J. Choe, *J. Electrochem. Soc.* **120**, 701 (1973).
11. T. Inagaki, J. Nakamura, and Y. Nakamura, *Japan. J. Appl. Phys.* **15**, 225 (1976).
12. T. Inagaki and M. Furukawa, *Thin Solid Films* **48**, 309 (1978).
13. Chandra var the Lal, Ph.D. thesis, Ohio University, (1979).
14. S. Y. Loyd and V. E. Miller, *Phys. Rev. B* **10**, 2062 (1974).

JAN-13-2003 MON 15:19

FAX NO.

P. 15

31.DEC.2002 15:30

NO.207 P.17/17

¹T. And, *J. Phys. Soc. Jpn.* 15, 974 (1960).

²G. P. Lyubchenko and V. K. Melnikovich, *Opt. Spectrosc.* 29, 53 (1965).

³J. L. Jacques and G. Bardet, *J. Phys. Chem. Solids* 26, 1041 (1975).

⁴K. Nakagawa, T. Sasaki, T. Arai, and I. Imai, *J. Phys. Soc. Jpn.* 13, 294 (1958).

⁵C. Bradshaw and A. J. Hughes, *Thin Solid Films* 23, 25 (1976).

⁶J. M. Ziman, *Electrons and Phonons* (Oxford, London, 1967), p. 234.

⁷E. H. Pursey, *The Hall Effect and Semiconductor Physics* (Dover, New York, 1964), p. 146.

⁸D. F. Morgan and J. A. Wright, *Brit. J. Appl. Phys.* 17, 247 (1966).

⁹D. A. Marley and R. C. Doherty, *Phys. Rev. A* 240, 304 (1963).

¹⁰L. Pottas, *Phys. Rev.* 206, 1508 (1966).

¹¹C. S. Khamis, *Optical Properties of Thin Solid Films* (Dover, New York, 1967), p. 74.

¹²E. Burstein, *Phys. Rev.* 93, 632 (1954).

¹³B. E. Kohlen, *J. Phys. Chem. Solids* 24, 1337 (1963).

¹⁴J. A. Scharf, *J. Phys. Chem. Solids* 23, 531 (1974).

¹⁵W. G. Spitzer and H. Y. Fan, *Phys. Rev.* 156, 813 (1957).

JAN-13-2003 MON 15:19

FAX NO.

31.DEC.2002 15:43

NO.208

P.1/8

(2)

Attachment 2

Electrical properties of highly conducting and transparent thin films of magnetron sputtered SnO_2

R. G. Goodridge, J. B. Webb, and D. F. Williams

Semiconductor Research Group, Division of Chemistry, National Research Council of Canada, 120 Sussex Drive, Ottawa, Ontario, K1A 0R6, Canada

(Received 20 July 1994; accepted for publication 15 October 1994)

Conducting and transparent thin films (60 and 120 nm) of the oxide were prepared by reactive rf planar magnetron sputtering of an undoped hot-pressed polycrystalline tin oxide target onto unheated substrates. The effects of the oxygen partial pressure on the room-temperature electrical properties of the films were studied. The properties vary markedly with, for example, the value of resistivity ranging from a high of $\sim 6 \times 10^{-1} \Omega \text{ cm}$ to a minimum value of about $3 \times 10^{-3} \Omega \text{ cm}$. This minimum is the lowest value of resistivity reported for undoped films prepared on unheated substrates. These films have optical transmittances greater than 50% averaged between 350 and 550 nm.

INTRODUCTION

Transparent conducting tin oxide (SnO_2 ; $n=2$) thin films have been studied for many years¹⁻³ due to their potential applications as heat mirrors, display systems, solar cells, etc. The films may be produced by any number of methods, including chemical vapor deposition,⁴⁻⁶ spray pyrolysis,⁷ oxidation of evaporated thin films of tin,⁸ or reactive dc ion sputtering of the targets.⁹ If planar magnetron sputtering has also been used to prepare SnO_2 films¹⁰⁻¹² from Sb-doped SnO_2 sintered targets. The high degree of process control, large area coverage, and high deposition rates has made this technique particularly attractive.

In the work reported above, to obtain high conductivity values as well as high values of transmittance, the methods require either that the doped/undoped SnO_2 films be deposited onto heated substrates, or that there be some postdeposition annealing of the films. The resulting films deposited under optimum conditions exhibit resistivities in the range of 10^{-2} – $10^{-3} \Omega \text{ cm}$ and transmittances greater than 50% between 350–550 nm. However, Buchanan *et al.*^{13,14} and Webb *et al.*¹⁵ have shown that transparent highly conducting thin films of indium tin oxide and zinc oxide, respectively, can be deposited on unheated substrates by reactive rf planar magnetron sputtering.

In this paper we report the preliminary results of our investigation into the deposition by reactive magnetron sputtering of SnO_2 films on unheated substrates. It is found that films can be deposited which exhibit resistivities of $3 \times 10^{-3} \Omega \text{ cm}$ and transmittances greater than 50%. This value of resistivity is among the lowest yet reported for tin oxide films. Furthermore, the films require no postdeposition treatment to achieve these characteristics. This should be compared to the optimum value of $2 \times 10^{-3} \Omega \text{ cm}$ obtained for Sb-doped SnO_2 films of comparable thickness, prepared on heated substrates by the same method.¹⁰

PREPARATION

The sputtering system consists of a cryopumped stainless-steel vacuum chamber equipped with a liquid nitrogen trap (base pressure $3 \times 10^{-7} \text{ Torr}$), an rf power supply coupled to both an automatic impedance matching network,

and a feedback system which maintains the target self-bias constant at the chosen rf power. The target, mounted horizontally in the chamber floor, is a hot-pressed SnO_2 (99.99% pure) disk of 10 cm diameter (Materials Research Corporation) silver-epoxy bonded to a cooling plate. The target-substrate separation is 7 cm. The sputtering and reactive gases, argon (99.999% pure) and oxygen, respectively, are individually controlled by needle valves and enter the chamber together. The incoming stream of gas is directed upwards and away from the target. The gas pressure is measured by an ionization gauge (below $5 \times 10^{-4} \text{ Torr}$) and by a Granville-Phillips capacitron gauge ($> 1 \times 10^{-3} \text{ Torr}$).

A typical film was prepared in the following manner. Having pumped down the chamber from atmospheric pressure to a throttled pressure of $5 \times 10^{-7} \text{ Torr}$, the target was sputtered in pure argon, onto a shutter at a pressure of $5 \times 10^{-3} \text{ Torr}$ for 10 min, with an rf power of 100 W. The chamber was then evacuated to below 10^{-4} Torr before setting the oxygen partial pressure. After the gas pressure stabilized ($\approx 15 \text{ min}$), argon was reintroduced to give the required total gas pressure of $5 \times 10^{-3} \text{ Torr}$. In every case for the film deposition the plasma was ignited at a pressure of $2.5 \times 10^{-2} \text{ Torr}$, with an rf power setting of 20 W and then set at 50 W, with minimal reflected power.

All substrates used were Pyrex glass, which had been ultrasonically cleaned in an alcohol solution, rinsed in deionized water and then washed in an isopropyl alcohol just before use.

RESULTS

Two series of films were produced on unheated substrates; one ~ 60 -nm thickness and the other ~ 120 nm. All films were deposited at the same rf power of 50 W and total gas pressure ($\text{Ar} + \text{O}_2 = 5 \times 10^{-3} \text{ Torr}$). This combination of power and total pressure yields a deposition rate of 1.2 nm/min.

Figure 1 and 2 show the variation of the room-temperature resistivity ρ , carrier concentration n , and Hall mobility μ_H with the oxygen partial pressure for films of 60- and 120-nm thickness, respectively. The 60-nm films, Fig. 1, show a sharp minimum in the resistivity ($3.2 \times 10^{-3} \Omega \text{ cm}$) for films

31.DEC.2002 15:43

NO. 288 P.2/8

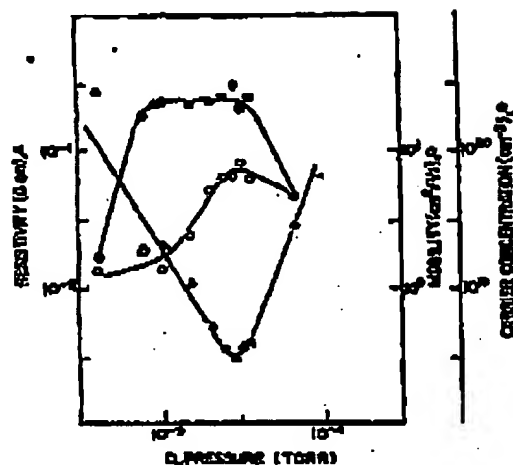


FIG. 1. Room-temperature variation of resistivity (Δ), mobility (\square), and carrier concentration (\bullet) with oxygen partial pressure for 60-nm-thick films.

deposited in an oxygen partial pressure of $(2.5-3) \times 10^{-5}$ Torr. All films deposited with the oxygen partial pressure in the region $(1-3.5) \times 10^{-5}$ Torr are strongly *n*-type with essentially the same value of n , i.e., $2.5 \times 10^{19} \text{ cm}^{-3}$. However, on either side of this region, n is observed to fall rapidly. As the oxygen partial pressure is increased beyond 10^{-4} Torr, μ_H rises to a peak value of approximately $7 \text{ cm}^2/\text{V s}$ at 3×10^{-4} Torr before decreasing.

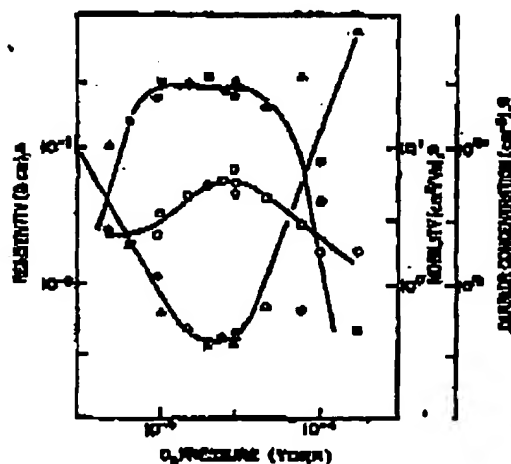


FIG. 2. Room-temperature variation of resistivity (Δ), mobility (\square), and carrier concentration (\bullet) with oxygen partial pressure for 120-nm-thick films.

2500

J. Appl. Phys., Vol. 87, No. 6, 15 March 1995

Downloaded 24 Dec 2002 to 271.72.48.2. Redistribution subject to AIP license or copyright; see http://jap.aip.org/japocopyright.jsp

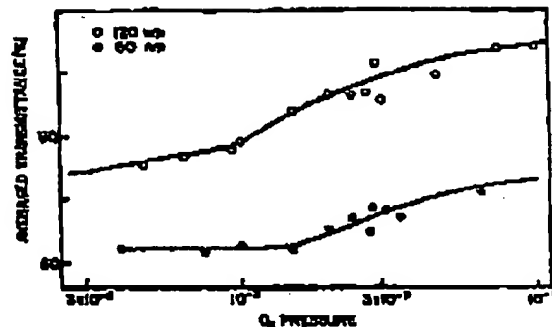


FIG. 3. Variation of the averaged transmittance (450-550 nm) with oxygen partial pressure. (\circ) 120-nm-thick films; (\bullet) 60-nm-thick films.

In Fig. 2, it is seen that the 120-nm-thick films show the same general variations of ρ , n , and μ_H with oxygen partial pressure as is observed for 60-nm-thick films. However, the resistivity minimum [$3.7 \times 10^{-3} \Omega \text{ cm}$] is now somewhat broader [$(1.7-3) \times 10^{-3} \text{ Torr}$]. The region of constant n is the same (Fig. 1), but the value of the plateau is higher, i.e., $2.8 \times 10^{19} \text{ cm}^{-3}$. Again, μ_H is a maximum at an oxygen partial pressure of 3×10^{-4} Torr, but the peak value is now slightly lower, i.e., $6 \text{ cm}^2/\text{V s}$.

The variation of the average value of transmittance (450-550 nm) with oxygen partial pressure for both film thicknesses is plotted in Fig. 3. It can be seen that for both cases there is a marked increase in the observed average transmittance for films deposited with oxygen partial pressures above 1×10^{-4} Torr. It is interesting to note that this pressure coincides with the beginning of the region of constant n and the rise in μ_H observed for both film series. Furthermore, as can readily be seen, between 650 and 550 nm, 120-nm-thick films exhibit higher values of averaged transmittance than 60-nm-thick films. (For example, at 3×10^{-4} Torr T_{avg} is 94%, compared to 84%.)

DISCUSSION

Films deposited in relatively low oxygen partial pressure conditions visually appeared to be yellowish brown in color. This is probably indicative of the presence of an SnO phase.¹⁰ As the oxygen partial pressure is increased, the films become clearer (Fig. 3). Suzuki and Mizutani have reported that the amount of the SnO phase is reduced with increasing oxygen partial pressure.¹⁰ These observations indicate that at low oxygen partial pressures, the film composition is dominated by the SnO phase and that, as the oxygen pressure is increased, this phase gives way to SnO_2 . Thus, the observed variation of ρ with oxygen partial pressure could be explained by the presence of mixtures of a SnO and a SnO_2 phase. The resistivity reaches a minimum when the film composition has the optimum concentration of oxygen vacancies. Although the change in mobility by a factor of ~ 3 is in the direction to give decreasing resistivity, it is too small to account for the observed two orders of magnitude decrease.

Goodfriend, Webb, and Williams

2509

JAN-13-2003 MON 15:20

FAX NO.

P. 18

31. DEC. 2002 15:44

NO. 228 P. 3/8

The rise in mobility, in films prepared under oxygen pressures of up to 3×10^{-3} Torr, suggests a consistent improvement in the film crystallinity, since it has been recognized that increased oxygen partial pressures can promote the growth of crystallites.¹⁰ Above an oxygen partial pressure of 3×10^{-3} Torr, the resistivity increases rapidly. The rise in ρ is probably due to the decreased number of oxygen vacancies which reduces n , since again the change in μ_H is not large. It can be argued that the decrease in mobility, above 3×10^{-3} Torr, is due to increased grain scattering caused by a larger number of smaller crystallites.

SUMMARY

Conducting and optically transparent thin films of SnO_2 have been prepared on unheated substrates by reactive rf planar magnetron sputtering. Although the complete dependence of film properties on deposition conditions have not been studied at present, it has already been found that with an rf power of 50 W, a target-substrate separation of 7 cm, an argon sputtering pressure of 5×10^{-3} Torr containing an oxygen partial pressure of $\approx 2.5 \times 10^{-3}$ Torr, a film with high transparency ($> 80\%$), and resistivity lower than any previously prepared on unheated substrates can be obtained. Specifically the films deposited under the above conditions exhibit values of ρ of $\approx 3 \times 10^{-3} \Omega \text{ cm}$, n of the order of $2.5 \times 10^{20} \text{ cm}^{-3}$, and Hall mobility values of $\approx 7 \text{ cm}^2/\text{V s}$. These values compare quite favorably with those found for

the optimum films produced by Suzuki and Mizuhashi² ($\rho = 3 \times 10^{-3} \Omega \text{ cm}$, $n \approx 3 \times 10^{20} \text{ cm}^{-3}$, $\mu_H = 10 \text{ cm}^2/\text{V s}$) on heated substrates from an Sb-doped SnO_2 target. The resistivity dependence on the partial pressure of oxygen shows a minimum with the above conditions. Increasing resistivity with increasing or decreasing oxygen partial pressures are associated both with changes in the film composition and overall crystallinity.

¹J. C. Manifacier, *Thin Solid Films* 96, 287 (1982).

²K. L. Chopra and S. K. Das, *Thin Film Solar Cells* (Plenum, New York, 1983), p. 326.

³A. G. Lee, M. S. Lee, J. E. Claydon, and J. H. Fisher, *Thin Solid Films* 208, 143 (1992).

⁴M. S. Murty, O. K. Shrivastava, and S. K. Jaiswal, *Thin Solid Films* 24, 347 (1982).

⁵B. Swarick, A. Ramer, V. Datta, and K. L. Chopra, *J. Appl. Phys.* 53, 1615 (1982).

⁶V. F. Hale and M. Mitra, *Thin Solid Films* 92, 133 (1982).

⁷G. Busch-Schweinitz, L. Krol-Schweinitz, and A. Mielke, *Thin Solid Films* 133, 315 (1985).

⁸K. Suzuki, M. Mizuhashi, and H. Sakata, *Japan. J. Appl. Phys.* 16, 158 (1977).

⁹K. Suzuki and M. Mizuhashi, *Thin Solid Films* 97, 119 (1982).

¹⁰M. Buchanan, J. R. Webb, and D. F. Williams, *Appl. Phys. Lett.* 37, 213 (1980).

¹¹M. Buchanan, J. R. Webb, and D. F. Williams, *Thin Solid Films* 24, 373 (1981).

¹²J. R. Webb, D. F. Williams, and M. Buchanan, *Appl. Phys. Lett.* 39, 640 (1981).

Attachment 3

PHYSICAL REVIEW B

VOLUME 50, NUMBER 6

15 SEPTEMBER 1994

Defect levels of SnO_2

John Robertson

Department of Physics, University of Illinois, Urbana, Illinois 61801
 and Central Electricity Research Laboratories, Leatherhead,
 Surrey KT20 7EE, United Kingdom

(Received 27 October 1993; revised manuscript received 2 March 1994)

A theory of the major chemical defects of impurity and vacancy levels in SnO_2 is presented, based on a tight-binding Green's-function calculation. Our results account for the shallowness of levels associated with substitutional Sb_{Sn} and Fe_{Sn} centers and the ionized oxygen vacancy. The behavior of defects in SnO_2 and SiO_2 is compared and discussed in terms of their bulk electronic structures and different coordination.

SnO_2 is a refractory oxide with a wide 3.6-eV optical gap and a conduction-band minimum of low effective mass,^{1,2} so it has important applications as a transparent window-electrode and as a conducting ceramic.³ Substitutional arsenic or fluorine doping or a deficiency of oxygen produce shallow levels in SnO_2 , while similar centers in the isovalent oxide SiO_2 are deep or inert. In this note we use the results of a tight-binding Green's-function calculation to predict the relative ordering of deep levels associated with n and p -bonded substitutional impurities in SnO_2 . We then show why Sb_{Sn} and Fe_{Sn} sites and the oxygen vacancy V_{O} are shallow in SnO_2 and contrast this with the behavior of defects in SiO_2 in terms of differences in bonding and lattice relaxation at defect sites.

SnO_2 is 6S coordinated and fairly ionic. Thus, its Γ_1^+ conduction-band minimum is largely Sn p -like while its Γ_3^- valence-band maximum is O-like and localized on the p orbitals lying normal to the plane of the three O-Sn bonds.⁴ SnO_2 is 4:2 coordinated and also has an O p -like upper valence band. While the bonding in SnO_2 can be represented in terms of covalent bonds, the higher coordination of SnO_2 is consistent with more ionic bonding.

Deep levels arise if the defect potential is sufficiently strong. In this limit it is believed that the central-cell potential alone determines the energy levels.⁵ As for SiO_2 ,⁶ we calculate the energies of deep levels by the tight-binding Green's-function method, retaining only the central-cell potential and neglecting initially any lattice relaxation. The Sn site is distorted octahedral D_{2h} , so we expect levels of p -like A_1^+ , and p -like B_1^- , B_2^- , and B_3^- symmetry. The oxygen site is distorted tetrahedral T_d , giving one p - and p -like A_1 level and p -like B_1 and B_2 levels. The variations of defect energy with impurity potential are shown in Figs. 1 and 2. An element forms a deep level if a solution is found in the gap for that defect potential, otherwise the long-range part of any Coulombic potential binds shallow levels. The figures place impurity levels in a specific order allowing chemical trends to be identified and possible systematic errors to be recognized from limited experimental data.

The curves for Sn site impurities are A_1^+ and donor-like A_1^- (Fig. 1). The p -like donor curves (not shown) lie above the A_1^- curves for all potentials, as are unoccupied, and all the acceptor-like parts of the curves lie entirely in the valence band. The heavier group V elements like Sb are predicted to be shallow, as seen experimentally,⁷ while the lighter P is

predicted to be just deep. All Sn site acceptors are predicted to be shallow. This is in disagreement with experiments where group III impurities in SnO_2 and tetrahedral GeO_2 are deep.⁷ However, these centers are anionic, the hole is localized on one of the six oxygen sites adjacent to the impurity, as discussed shortly.

The important levels associated with substitutional impurities at the oxygen site are the B_1^- p -like acceptor levels and A_1^- p -like donor levels. The B_1^- acceptor levels lie above all other acceptor-like levels and so trap any holes. As the B_1^- state is p , nonbonding and impurity-like, its energy lies close to that of the impurity p orbital. Figure 2 predicts most oxygen-site acceptors to be deep. Fluorine is the only possible oxygen-site donor, and its A_1^- level is calculated to be shallow (not shown), as seen experimentally.⁸ Other halogens cannot act as donors because their p orbital energies lie above that of oxygen and they are too electronegative.

A vacancy corresponds to an infinite defect potential in the tight-binding method. We find all levels of the neutral vacancy to be resonances in the bands (Fig. 3). The V_{O} vacancy V_{O} is not found experimentally because of its large charge. V_{O} is usually positively charged, and its Coulombic well now binds shallow levels, as seen experimentally.⁹

It is instructive to compare the present results with those of Robertson, Robertson, and Dow⁶ for SiO_2 as in general

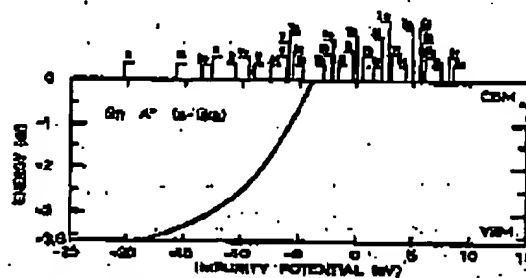


FIG. 1. Predicted energies of deep A_1^+ levels at the Sn site, between the valence-band maximum (VBM) and conduction-band minimum (CBM). The p -like B_1^- , B_2^- , and B_3^- levels (not shown) all lie higher.

JAN-13-2003 MON 15:21

FAX NO.

P. 20

31.DEC.2002 15:23

NO.207 P.5/17

20

BRIEF REPORTS

3221

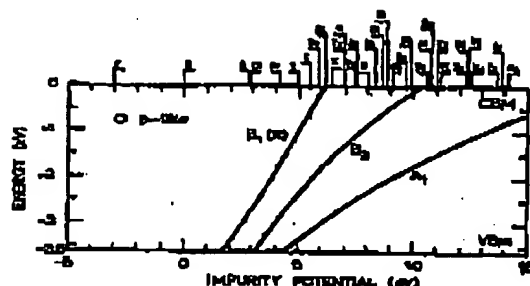


FIG. 2. Predicted energies of deep levels of p-type A_1 (π), A_2 , and A_3 symmetry at the O site.

Impurities behave quite differently in SnO_2 and SiO_2 in spite of Sn and Si both being semimetals. In detail, for the valence, SnO_2/P_2 is a shallow donor while $\text{SiO}_2/\text{P}_2^+$ is very deep,¹ for isoelectronic impurities SnO_2/Sb_2 is shallow while SiO_2/P_2 is deep, and SnO_2/P_2 is shallow while F does not produce gap states in SiO_2 . In common trivalent impurity centers like SnO_2/Al_3 and SiO_2/Al_3 are both deep with the hole localized on an adjacent oxygen in each case.^{2,3} We now account for these differences in terms of the bulk electronic structure and different coordinations. SnO_2 has a gap $E_g = 3.6$ eV, and its conduction-band minimum has an effective mass $m_c = 0.3$ in (Ref. 2) and 30% for constant,⁴ so shallow donors are truly delocalized, with radius ~ 20 Å. In SiO_2 , $E_g = 9$ eV and even nominally shallow levels have sizeable binding energies (~ 1.5 eV, Ref. 3) and are quite localized. The valence-band maximum is made of oxygen π states in both compounds and covalently has a very high effective mass, over 10 in for SiO_2 and we calculate over 20 in for SnO_2 . Thus, nominally shallow hole states are strongly localized in both compounds.

The trends in donor levels associated with pentavalent impurities depend on the impurity potential or "threshold" at which the cation A^+ center enters the gap. More negative values favor shallower impurities. We find correctly that



FIG. 3. Calculated energy levels of V_O for (a) unreduced vacancy in SnO_2 , (b) unreduced vacancy in SiO_2 , (c) reduced V_O^+ center in SiO_2 (cf. text).

the isoelectronic centers SnO_2/Sb_2 and SiO_2/P_2 are shallow and deep, respectively, for two reasons. Firstly, the impurity potential is less for Sb_2 , -2.9 compared to -4.3 eV for P_2 , and secondly, the threshold is greater in SnO_2 , -3.3 compared to -2.0 eV in SiO_2 . The low threshold of SnO_2 arises from its remarkable broad conduction minimum. In contrast the A_1 threshold of SiO_2 is much higher, largely because of its higher electron mass. The delocalization of SnO_2/Sb_2 minimizes relaxation, while the localization of SiO_2/P_2 enhances the tendency of neighboring atoms to relax.

We calculate the levels of unreduced V_O in both SnO_2 and SiO_2 to be shallow (Fig. 3). Experimentally, V_O^+ is shallow in SnO_2 but very deep in SiO_2 . V_O^+ is a model for the E' center observed by ESR in SiO_2 .¹⁰ The single defect electron is found to be preferentially localized on only one of the two Si dangling bonds of the vacancy, and it is assumed that the positive Si site has relaxed away from the vacancy towards a planar configuration. The low electron coordination allows such relaxation to occur in SiO_2 by bond rotation without any change in bond length, but this would not be possible in the SnO_2 lattice. The relaxation strongly affects the associated levels, and the occupied level of SiO_2/V_O^+ is very deep, near midgap. The depth of SiO_2/V_O^+ is largely attributable to self-energy shifts in our model of this center.⁸ Self-energy shifts are introduced as Si sp^3 hybrids of a dangling bond to model the absence of the bulk Si-O overlap repulsion. Just as deep states are bound by large central-cell potentials, strong self-energy shifts at dangling bonds can force these levels deep. The shifts are much smaller in SnO_2 than in SiO_2 (Ref. 11) and are insufficient to create a deep vacancy state. Thus, SnO_2/V_O^+ remains shallow.

The doping of SnO_2 by P_2 is also related to the different responses of the SnO_2 and SiO_2 lattices to gross oxygen deficiency. While the $4d$ coordination around an oxygen vacancy in SnO_2 is that of the bulk, oxygen deficiency in amorphous SiO_2 occurs by breaking chemical order, by the formation of covalent Si-Si bonds. These maintain a subvalent valence so A_1 remains in midgap.

SnO_2/P_2 is shallow donor level in SnO_2 but shallow in SiO_2 has no gap level. We suggest that this indicates that fluorine enters a true substitutional site in SnO_2 but not in SiO_2 ; it takes advantage of the low O coordination by substituting two nonbridging $\pi\text{Si}-\text{F}$ sites for one bridging oxygen:



Valence is saturated at such fluorine centers and no gap levels result.

The similar behavior of equivalent impurities in SiO_2 and SnO_2 is largely due to O $p\pi$ states forming the upper valence band of both oxides. In both oxides Al_3 or In_3 centers cause the hole to localize on one of the adjacent oxygens.^{12,13} We calculate that SnO_2/In_3 should be shallow. However, such a state is strongly localized due to the high hole mass of $p\pi$ states. Electron-lattice coupling further localizes the hole onto a single oxygen π orbital in both compounds. It is reassuring that calculations based on the extensive previous model of charged ions also conclude that the holes are trapped in $p\pi$ states.⁷

In conclusion, SnO_2 is a good n -type semiconductor in

JAN-13-2003 MON 15:21

FAX NO.

P. 21

31.DEC.2002 15:24

NO.287

P.6/17

3322

BRIEF REPORTS

25

optics of its ionic bonding because it has a low mass s -like conduction-band minimum. In contrast SiO_2 is covalent but insulating because the conduction minimum has a larger mass, and its low coordination allows chemical effects to dominate most of its defect states, in the sense that there is a strong tendency towards covalent bonding at its defects. In this regard, a comparative experimental study of defects in

the 6:3 and 4:3 coordinated polymorphs of GeO_2 and SnO_2 would be most interesting.

ACKNOWLEDGMENT

The author is grateful for the support of the U.S. Army Research Office Grant No. ARO-DAG-01-K-00681.

Present address:

1. J. Robertson, *J. Phys. C* **12**, 4767 (1979).
 2. T. Agulyn, *Phys. Status Solidi* **43**, 11 (1977).
 3. M. Zundel and I. P. Martin, *J. Electrochem. Soc.* **123**, 199C (1976); **123**, 239C (1976); **123**, 233C (1976).
 4. J. Robertson, P. Voni, D. J. Wolford, and I. D. Dow, *Phys. Rev. Lett.* **44**, 818 (1980).
 5. A. Elmberg, J. Robertson, and I. D. Dow, *Phys. Rev. B* **29**, 2216 (1984).
 6. The tight-binding Hamiltonian is the same as in Ref. 1, except the orbital energies are $\text{Sn } s = 1.7 \text{ eV}$, $p = 9.6 \text{ eV}$, $\text{O } s = -16.9 \text{ eV}$, and $p = -1.0 \text{ eV}$ and the first-neighbor two-center interactions $V(\text{Sn } s, \text{O } p) = 2.0 \text{ eV}$ and $V(\text{O } s, \text{Sn } p) = 2.30 \text{ eV}$.
 7. M. Szeferman, R. H. Barren, O. K. Gilman, and D. P. Minami, *Phys. Rev. B* **13**, 1950 (1976); M. Szeferman, O. K. Gilman, and

- R. H. Barren, *ibid.* **16**, 37 (1977); R. B. Rowell, T. J. Welch, O. K. Gilman, and M. Szeferman, *ibid.* **12**, 4376 (1976); D. Zwingel, *Phys. Status Solidi B* **77**, 571 (1976); D. Zwingel and B. Mooser, *J. Lumin.* **12**, 441 (1976).
 8. P. O'Reilly and J. Robertson, *Phys. Rev. B* **27**, 5780 (1983).
 9. L. Griscom, P. C. Taylor, D. A. Wiersma, and R. L. Bray, *J. Chem. Phys.* **43**, 5159 (1965).
 10. L. Ye and W. R. Fowler, *Phys. Rev. B* **11**, 2117 (1975).
 11. A self-energy shift of 4.95 eV of $3d$ orbitals is used in SnO_2 . This shifts the conduction-band edges of SnO_2 and Sn . A much smaller shift of $\text{Sn } s$ orbitals of 1.2 eV is needed in SnO_2 . This is the shift with respect to the free-atom energies of Sn and O needed to give the experimental gap. As this is insignificant to send SnO_2 deep, in effect self-energy shifts are not important in our description of deep centers in SnO_2 .

JAN-13-2003 MON 15:22

FAX NO.

P. 01/07

1 DEC 2002 15:24

NO. 287 P. 7/17

Attachment A

W.D. Kingery, H.K. Bowen and D.R. Uhlmann
 "Introduction to Ceramics" John Wiley & Sons, New York, 1975.

INTRODUCTION TO CERAMICS

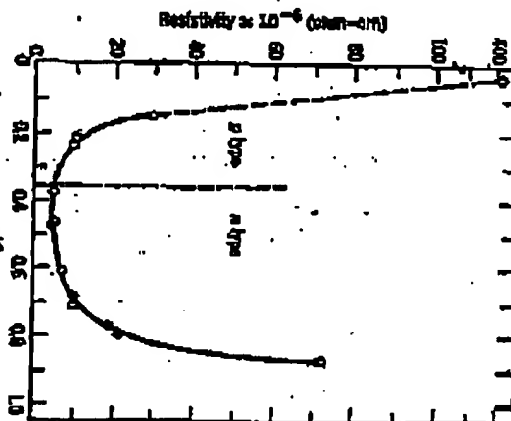


Fig. 17.21. The effect of P_{O_2}/P_{tot} on resistivity at 200°C for glasses containing 5% FeO-5% B₂O₃. From H. K. Bowen, J. E. Eickert, Jr., and D. R. Uhlmann, *J. Non-Crystalline Solids*, 11, 21 (1970).

17.6 Nonstoichiometric and Defect-Controlled Electronic Conduction

Most oxide semiconductors are either doped to create extrinsic defects or are annealed under conditions in which they become nonstoichiometric. These effects have been carefully studied in many oxides, but the precise nature of the low mobility values is often difficult to interpret. Reported conductivities are often, at variance because the variable impurity effects and fast thermal history overwhelm other effects. In this section we consider several electronically conducting ceramics to point out important features in their behavior. A partial list of impurity semiconductors is given in Table 17.6. The strong effect of impurities on the properties of semiconductors results from the fact that the impurity atoms introduce new localized energy levels for electrons intermediate between the valence band and the conduction band. If the new energy levels are unoccupied and lie close to the energy of the top of the valence band, it is easy to excite electrons out of the filled band into these new acceptor levels. This leaves an electron hole in the valence band that can contribute to electrical conductivity. Positive carrier (p-type) oxide conductors most commonly arise as a result of nonstoichiometric com-

ELECTRICAL CONDUCTIVITY

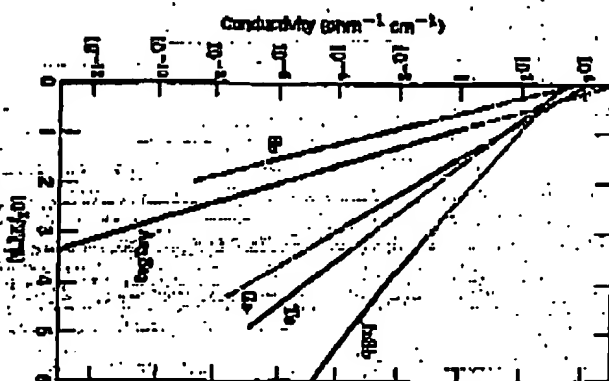


Fig. 17.23. Intrinsic electrical conductivity of various oxides as a function of $1/T$. Data of various authors are summarized from C. C. Smith et al., *J. Non-Crystalline Solids*, 1, 21 (1970).

pulsion with a decreased metal content (O_{2-x} is an example) and are sometimes called defect semiconductors. If the impurity addition have filled electron levels close to the energy level of the conduction band, electrons may be excited from impurity atoms into the conduction band; these are called donor levels. The electron excited into the conduction band is able to contribute to the conductivity. Negative carrier (n-type) oxide conductors most commonly result from a nonstoichiometric composition with an excess metal content ($Zn_{1+x}O$ is an example) and are sometimes called excess semiconductors.

Stoichiometric oxides. For SnO_2 , density, lattice parameter, and conductivity data have demonstrated that the mass action relationships which we have discussed in Chapter 4 are valid. Single crystals were reduced at 1200 to 1400°C in gas mixtures ($P_{O_2} = 10^{-7}$ to 10^{-9} atm) in

*H. Yamaoka and G. R. Miller, *J. Solid State Chem.*, 6, 129 (1971).

JAN-13-2003 MON 15:23

FAX NO.

P. 02/07

31 DEC 2002 15:25

No. 287

P. 8/17

Fig. 17.29. Relation between electrical conductivity and activation energy E for conduction for various crystalline and amorphous semiconductors. From R. Saha, J. Non-Cryst. Solids, 4, 1 (1970).

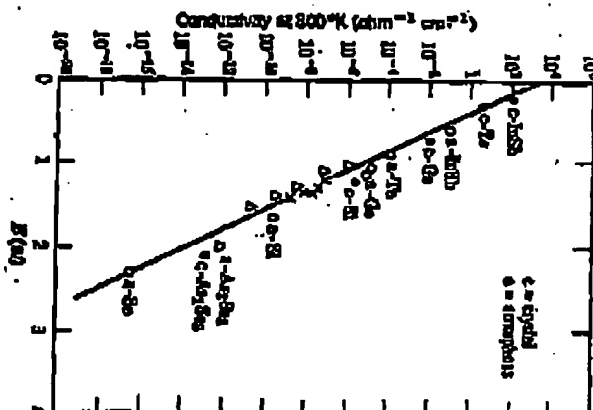


Table 17.6. Partial List of Semiconductors

s-Type		
TiO ₂	Nb ₂ O ₅	CeO ₂
Y ₂ O ₃	MoO ₃	CaSe
UO ₂	CrO ₂	SnO ₂
ZnO	Ag ₂ S	CS ₂
		W ₂ O ₅
p-Type		
Ag ₂ O	Cu ₂ O	Bi ₂ Te ₃
Cu ₂ O	SnO ₂	Bi ₂ Se ₃
MnO	NiO	Fe ₂ O ₃
		Te
		Bi ₂ Te ₃
		TeO ₂
Amorphous		
Al ₂ O ₃	SiO ₂	Si
Mn ₂ O ₃	Fe ₂ O ₃	Ge
Co ₂ O ₃	Fe ₂ O ₃	Si

ELECTRICAL CONDUCTIVITY

891

which the following reduction reaction is assumed:



The equilibrium constant for the reaction is,

$$\frac{[V_{O}^{\bullet}][e^-]^2}{[O_2]} = K(T) \quad (17.58)$$

and from this the concentration of free electrons for reduction is given as

$$[e^-] = (2K(T))^{1/2} P_{O_2}^{-1/4} \exp\left(-\frac{AE}{2kT}\right) \quad (17.59)$$

The experimental vaporization of Eq. 17.59 is shown in Fig. 17.30a, where electron concentration data were obtained from Hall measurements (Fig. 17.53). The temperature dependences of Eq. 17.59 (Fig. 17.30b) indicate that the mobility to create an oxygen vacancy and two conduction-band electrons is 5.76 eV (113 kcal/mole). The defect model given in Fig. 17.57 is confirmed by comparison of measured crystalline densities on quenched specimens and calculated densities (Fig. 17.30c). In this case the oxygen vacancies become doubly ionized donors of electrons to the conduction band. The mobility of the electrons at room temperature is 6 cm²/V-sec.

Zinc Oxide. When ZnO is heated in a reducing atmosphere in which zinc gas is present, the zinc content of the oxide increases to form an

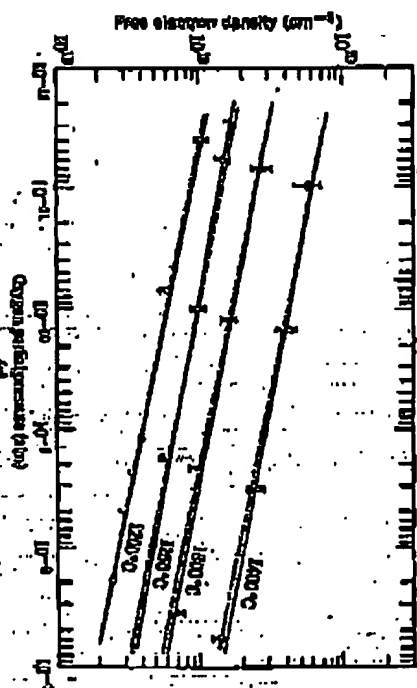


Fig. 17.31. (a) Concentration of free electrons as a function of oxygen pressure in ZnO. Dashed lines indicate $P_{O_2}^{1/4}$ dependence.

JAN-13-2003 MON 15:23

FAX NO.

31 DEC 2002 15:44

NO. 208 P. 4/8

Characterization of rf-sputtered SnO_2 thin films by electron microscopy, Hall-effect measurement, and Mössbauer spectrometry

Bert Eklund and Cezar G. Grigoras

Physics Department, Chalmers University of Technology and University of Gothenburg, S-413 45 Gothenburg, Sweden

Agnesa Gaidal and Lars-Olof Hagström

Physics Department, Uppsala University Box 130, S-751 21 Uppsala, Sweden

(Received 9 July 1999; accepted for publication 23 August 1999)

SnO_2 films, made by reactive rf magnetron sputtering onto substrate glass, were studied by electron microscopy, Hall-effect measurements, and Mössbauer spectrometry. Transmission electron microscopy showed that the films were polycrystalline with a grain size of ~ 15 nm. Hall-effect measurements gave a sharp resistivity minimum (down to $2.9 \times 10^{-3} \Omega \text{ cm}$) and electron concentration maximum (up to $1.3 \times 10^{20} \text{ cm}^{-3}$) at a specific O_2/Ar gas-flow ratio during sputtering. Mössbauer spectrometry indicated that the most conducting films only consisted of the SnO_2 phase, and that a SnO phase appeared at low O_2/Ar ratio where it lowered the conductivity.

Attachment 5

1. INTRODUCTION AND SUMMARY

This paper presents results from electron microscopy, Hall-effect measurements, and Mössbauer spectrometry on nonstoichiometric tin oxide (SnO_2) thin films made by reactive rf magnetron sputtering onto substrate glass. The SnO_2 films combine luminous transmittance with infrared reflectance and electrical conductance.

Doped wide-band-gap semiconductors can be used in advanced construction within the architectural and automotive sectors,^{1,2} as transparent electrodes in display devices, as antistatic packaging materials, for gas sensing,³ and in many other fields of modern technology. The most interesting—up to at least most widely studied—materials are based on SnO_2 ,⁴ In_2O_3 ,⁵ and ZnO .⁶ These semiconductors are doped either by substitution or by nonstoichiometry. For the latter case, doubly ionized oxygen vacancies serve as n-type donors, as discussed for SnO_2 in Ref. 7.

Some of the previous authors recently investigated^{8–10} SnO_2 and found that coatings can be produced by high-rate magnetron sputtering in $\text{Ar} + \text{O}_2$ onto substrate glass⁸ and polyester.⁹ In Sec. II we outline a technique capable of yielding films with a luminous transmittance of $\sim 75\%$ and a resistivity of $\sim 3 \times 10^{-3} \Omega \text{ cm}$. The optical and electrical properties could be accounted for with an effective mass model¹¹ for n-doped semiconductors well above the Mott critical density and accounting for limited impurity scattering of the free electrons. Our earlier reported work did not address microstructural characterization in any detail, and clearly there is a need for more work on this subject. Thus the present work can be motivated from a basic physics point of view, because of its bearing on the theoretical model, as well as from a technological point of view because of the numerous application possibilities for SnO_2 thin films.

Section III of this paper deals with microstructure studies by transmission electron microscopy. It is shown that our SnO_2 films are polycrystalline with a grain size of about 15 nm, and that the diffusion patterns from the films with the lowest resistivity are consistent with a single-phase SnO_2 .

Structure. Section IV gives results of Hall-effect measurements. A sharp minimum of the resistivity (down to $2.9 \times 10^{-3} \Omega \text{ cm}$) and a maximum in the carrier concentration (up to $1.3 \times 10^{20} \text{ cm}^{-3}$) take place at a specific O_2/Ar gas-flow ratio. Section V reports data from Mössbauer spectrometry. In Sec. VI we attempt a unifying discussion of the various experimental results. It is found from Mössbauer spectrometry that the films with lowest resistivity only consist of the SnO_2 phase, and that a SnO phase appears at low O_2/Ar gas-flow ratios where it increases the resistivity. The carrier shift of the SnO_2 phase increases with decreasing O_2/Ar gas-flow ratio, and it is argued that this points at a larger number of oxygen vacancies in the film. The microstructural characterization gives credence to the earlier⁸ presented theoretical model for the optical and electrical properties of SnO_2 .

II. THIN-FILM PREPARATION

A detailed description of the preparation of SnO_2 thin films is given in Ref. 8. In essence, the films were grown by reactive rf magnetron sputtering onto substrate glass in a box-type magnetron sputter.¹² After evacuation to $\sim 10^{-4}$ Torr by cryopumping, a mixture of Ar (99.997%) and O_2 (99.998%) was introduced via mass-flow-controlled inlets. Sputtering was conducted from a 10-cm-diam planar magnetron cathode powered by a 600-W supply (13.56 MHz) via a matched impedance matching network. The target was 99.999% pure Sn . The sputtering-chamber distance was 5 cm. Substrates were 0.1-cm-thick microscopy cover glasses and copper grids coated with carbon film.

All of the films were deposited at a power of 70 W and a total gas pressure of 4 mTorr. SnO_2 films with different properties were obtained by varying the O_2/Ar gas-flow ratio r . Specifically, films with a luminous transmittance obtained by averaging spectrophotometric data over the spectral efficiency of the eye of $\sim 75\%$ and an electrical dc resistivity of $\sim 3 \times 10^{-3} \Omega \text{ cm}$ were accomplished at $r = 6.5\%$. All of the films made for Hall-effect measurements

JAN-13-2003 MON 15:24

FAX NO.

31 DEC 2002 15:45

NO. 208 P. 5/8

and Mössbauer spectrometry had a thickness between 1.0 and 1.5 μm , whereas the films for electron microscopy had a thickness of about 0.12 μm .

III. ELECTRON MICROSCOPY AND ELECTRON DIFFRACTION

The microstructure was studied by transmission electron microscopy using a Philips EM 300 instrument operated at 100 keV. The specimens were prepared under conditions that gave highest transparency and contrast, as described in Sec. II and in Ref. 8.

The left-hand part of Fig. 1 shows a transmission electron micrograph in the dark-field mode for a SnO_2 film. The sizes of the illuminated spots yield that the sample is polycrystalline with grain size being ~ 15 nm in linear extent. We believe that the grain size depends on the film thickness and that thicker coatings, such as those used in study^{1,10} of optical and electrical properties, have a higher degree of crystallinity. Literature data¹²⁻¹⁵ on SnO_2 thin films made by reactive sputter deposition onto oxidized substrates show that either amorphous^{14,15} or crystalline¹² structures can appear, depending on the oxygen content during sputtering. We note that the grain size of our SnO_2 films is roughly a factor of 2 less than in transparent and conducting ZnO:Al films¹⁶ made by reactive sputtering onto unheated substrates and In_2O_3 films¹⁷ made by reactive s-beam evaporation onto substrates heated to 300 °C.

The right-hand part of Fig. 1 depicts an electron diffraction pattern with rings designated by (hkl) indices. The pattern is in full agreement with that expected for a tetragonal (see the structure (ASTM Card No. 21-1250), and no additional diffraction features^{18,19}—for example, due to a CaF_2 -type configuration¹⁹—could be discerned. No preferred orientation could be seen from the diffraction pattern.

IV. HALL-EFFECT MEASUREMENTS

Hall-effect data were taken at room temperatures with the van der Pauw technique²⁰ using fully computerized equipment capable of providing a magnetic field up to 0.5 T. The samples were 4.0×4.0 mm² in size, cut from the SnO_2 -coated glass substrates they were mounted onto a holder with copper foil electrodes attached by silver epoxy contacts ($\phi \sim 0.3$ mm square-areas) in the corners of the sample.

Figure 2 reports resistivity ρ , electron density n , and mobility μ as a function of gas composition specified by Γ . It is seen that ρ varies by about four orders of magnitude for $6.5 \text{ eV} < \Gamma < 7.4 \text{ eV}$, and that a well-defined minimum, down to $\sim 2.5 \times 10^{-3} \text{ } \Omega \text{ cm}$, occurs at $\Gamma \approx 6.5 \text{ eV}$. These results are in good agreement with our earlier¹ measurements, using a simple resistance probe, as well as with literature data^{14,15} on SnO_2 films made by reactive sputtering onto unheated substrates. The lowest resistivity, being $1.9 \times 10^{-3} \text{ } \Omega \text{ cm}$, was found¹⁴ by rf magnetron sputtering from a SnO_2 target in an applied magnetic field. We note in this context that resistivities down into the low $10^{-4} \text{ } \Omega \text{ cm}$ range have been obtained²¹⁻²³ in substitutionally doped SnO_2 , In_2O_3 , and ZnO .

Figure 2 also shows that the electron density displays a variation with Γ that mirrors the one in ρ , and that n has a maximum of $\sim 1.5 \times 10^{20} \text{ cm}^{-3}$. The corresponding oxygen deficiency, expressed as SnO_{2-x} , can be derived from the size of the SnO_2 unit cell²⁴ and the fact that each oxygen vacancy is expected²⁵ to release two electrons. We find $x \approx 3 \times 10^{-3}$ at maximum n .

The lower part of Fig. 2 shows that the mobility increases approximately linearly with increasing Γ ($\sim 10 \text{ cm}^2 \text{ V}^{-1} \text{ s}^{-1}$ for the gas composition yielding minimum ρ).

V. MÖSSBAUER SPECTROMETRY

Mössbauer spectra were taken with equipment of conventional constant acceleration type utilizing a vibrator with



FIG. 1. Dark-field transmission electron micrograph (left) and corresponding electron diffraction pattern (right) for a 0.12- μm -thick SnO_2 film. Horizontal bar indicates the magnification in the micrograph. Diffraction rings are designated by (hkl) indices.

JAN-13-2003 MON 15:24

FAX NO.

31 DEC 2002 15:45

NO. 208 P. 6/8

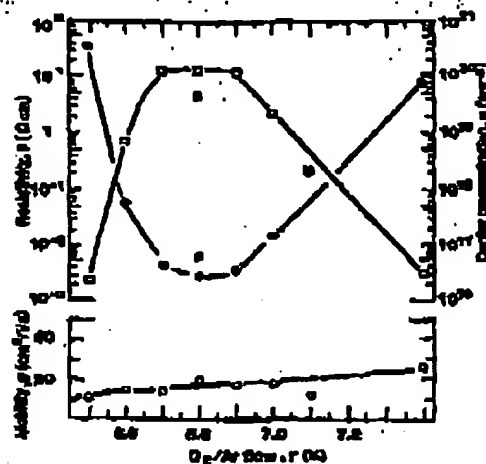


FIG. 3. Data from Hall-effect measurements on SnO_2 films grown deposited at different O_2/Ar gas-flow ratios. The various symbols refer to resistivity, carrier (squares) concentration, and mobility. The curves were drawn only to guide the eye.

a $5\text{-mCi } ^{60}\text{Co}$ source on one end and a ^{57}Co source on the other end for calibration. The linewidth of the tin source was 0.193 mm/s according to the manufacturer (Amersham Int. Ltd.). All Mössbauer measurements were performed at room temperature. For calibration, a natural cobalt film was used as the absorber. The Mössbauer spectra were recorded with the SnO_2 samples as absorbers. The spectra were folded and analyzed by use of a least-square fitting program.²¹

Values of the recoil-free factor f were determined for SnO_2 and SnO by measurements on reference samples (powder compacts) containing known amounts of the two oxides. The result was $f(\text{SnO}_2)/f(\text{SnO}) = 1.13 \pm 0.13$, which is in good agreement with literature data.²²

Figure 3 shows representative Mössbauer spectra for two SnO_2 films and one reference sample. It appears that the spectra are either a single doublet centered around 0.10 mm/s , corresponding to SnO_2 (or Sn^{4+}), or a superposition of two doublets centered around 0.10 and 2.50 mm/s , for which the latter one corresponds to SnO (or Sn^{2+}). In all spectra the doublet centered around 0.10 mm/s is dominating. Analogous Mössbauer spectra are found in the literature for SnO_2 films made by sputtering^{1,2,23,24} and evaporation.²⁵

The spectra were analyzed by computer,²¹ and the characteristic parameters are listed in Table I. Specifically, we report data for five SnO_2 films grown deposited with different F_2 for the reference sample of Fig. 1, and for an amorphous tin oxide sample described in Ref. 28. The parameters analyzed are the valley separation of each doublet (i.e., the quadrupole splitting Δ), the point around which the

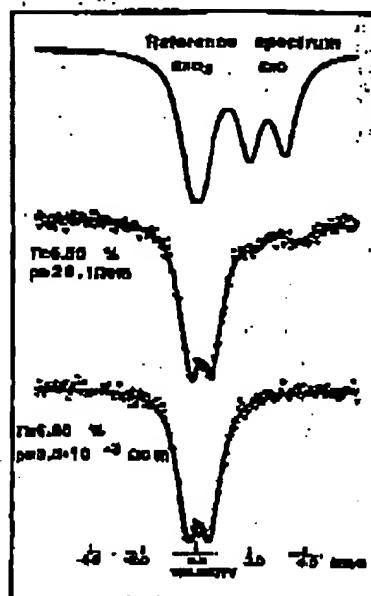


FIG. 4. Mössbauer spectra for SnO_2 films grown deposited at different gas-flow rates (F_2) and for one reference sample with known amounts of mixed SnO_2 and SnO . Relative areas (A_i) of the lines are given.

doublet is centered (i.e., the isomer shift δ), and the full linewidth at half maximum (denoted Γ). From the f -factor ratio given above and the relative intensities of the two doublets, we obtained the phase fractions of SnO_2 and SnO given in Table I.

VI. DISCUSSION

In this section we discuss the Mössbauer data, largely as summarized in Table I, in the light of the results from electron microscopy and Hall-effect measurements, and we make hypotheses regarding structure and doping mechanisms for our SnO_2 films.

The Mössbauer hyperfine parameters δ and Δ for the SnO_2 films are seen to be remarkably different from the corresponding quantities of the reference sample and, in fact, closer to the values reported in a characterization²⁶ of amorphous tin oxide. However, the linewidths of our SnO_2 films are much smaller than those reported²⁶ for the amorphous tin oxide and more similar to those for the crystalline powder reference sample. The fact that Δ differs from the corresponding value for crystalline tin oxide can be understood as an effect of small grain sizes ($\sim 15\text{ nm}$ as shown by electron microscopy) since varying $\text{Sn}-\text{O}$ bond lengths have²⁷ a

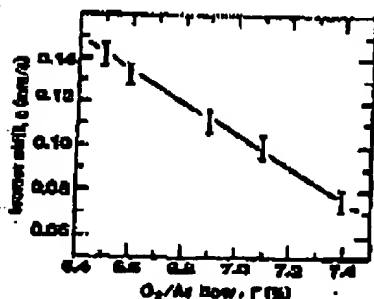
NO. 223 · P. 7/8

Chlorine ratio r (%)	FeCl ₂ (aq)			FeCl ₃ (aq)			Literature r (%)
	δ (mmole)	Δ (mmole)	Σ (%)	δ (mmole)	Δ (mmole)	Σ (%)	
0.5	0.143	0.51	80	2.536	1.43	20	0.83
0.6	0.133	0.82	95	2.296	1.68	7	0.80
0.9	0.111	0.84	100	—	—	—	0.81
7.1	0.103	0.16	103	—	—	—	0.99
7.6	0.076	0.83	100	—	—	—	0.91
a	-0.030	0.50	—	2.425	1.32	—	0.87
b	0.139	0.70	—	2.271	1.71	—	1.13

(1)

ACKNOWLEDGMENTS

1. C. G. Overman, *Elementary Synthetic Systems for Nitrogen and Oxygen Compounds* (SP-18, Baltimore, WA, 1977).
2. C. G. Overman and C. G. Overman, *Radical Syntheses Characteristic of Molecular Oxygen for the Transformation of Cyclic Olefins*, Baltimore, WA, 1978; *Org. Lett.* 20(15) 2695 (1978); *ibid.* (forth publication).
3. R. N. Adams, P. T. Mather, C. G. Overman, D. E. Williams, P. Taylor and B. C. Tisdale, *Polym. Prepr. Am. Chem. Soc.* 21, 677 (1979).
4. R. H. Hsieh, J. A. P. Eskin and C. K. Hoang, *Polym. Sci. Energy Mater.* 10, 230 (1979).
5. I. Fleming and C. G. Overman, *J. Appl. Phys.* 66, B132 (1968).
6. Z. C. Fu, I. Fleming, and C. G. Overman, *J. Appl. Phys.* 66, 3119 (1968).
7. M. J. Anzures and J. F. Martin, *J. Macromol. Sci.* 13, 1109 (1976); *ibid.* 19(1) (1976); *ibid.* 23, 231 (1978).



J. Appl. Phys., Vol. 62, No. 12, 15 December 1990

NO. 268 P. 8/8

- [illegible]